THE JOURNAL OF PHYSICAL CHEMISTRY C

Article

Cite This: J. Phys. Chem. C 2019, 123, 1610−1618

pubs.acs.org/JPCC

Simulation Study of the Capacitance and Charging Mechanisms of Ionic Liquid Mixtures near Carbon Electrodes

Alta Fang* and Alex Smolyanitsky

Applied Chemicals and Materials Division, National Institute of Standards and Technology, Boulder, Colorado 80305, United States

Supporting Information

ABSTRACT: The performance of electric double-layer capacitors is strongly influenced by the choice of electrolyte, and electrolytes comprised of ionic liquid mixtures have shown promise for enabling high energy densities. Here we perform all-atom molecular dynamics simulations of ionic liquids containing 1-ethyl-3-methylimidazolium and different fractions of bis(trifluoromethylsulfonyl)imide and tetrafluoroborate, in conjunction with planar graphene sheets as electrodes. We demonstrate that relative ion−electrode van der Waals interactions play an important role in the population of ions adsorbed in the first interfacial layer near uncharged electrodes. Near charged electrodes, we find that the ionic liquid mixtures generally exhibit integral capacitances intermediate between the two pure ionic liquids. We characterize cumulative ion densities near electrodes carrying various surface charges, revealing different charging mechanisms for different ionic liquids, which we relate to the relative sizes of the ions. Finally, in the ionic liquid mixtures we identify an effective ion exchanging phenomenon wherein charging of the electrodes leads to different trends in the densities of the two types of anions in the first interfacial layer, which enhances counterion adsorption and improves capacitance at the negative electrode.

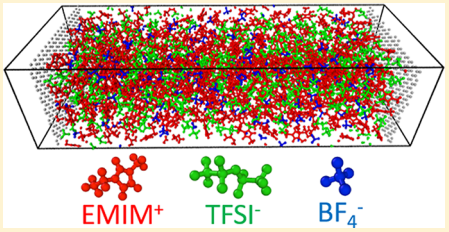

1. INTRODUCTION

Electric double-layer capacitors, also known as supercapacitors, are energy storage devices that offer lifetimes of up to a million cycles and high power densities of over 10 kW/kg, making them ideal for energy storage applications demanding durability and fast charging/discharging such as electric buses or cranes.[1−3] However, the energy density of a supercapacitor is typically below 10 Wh/kg,[4] limiting the further adoption of supercapacitors in many applications. The energy density of supercapacitors can be increased by increasing their capacitance or operating potential windows, both of which depend on the choice of electrolyte and electrode.[5,6] In order to rationally design improved devices, it is critical to develop a better understanding of the effects of the electrolyte and electrode on supercapacitor performance.

The use of room-temperature ionic liquids as electrolytes in supercapacitors offers the promise of high energy densities by enabling wide operating potential windows.[5] Furthermore, ionic liquids, which are comprised entirely of ions without any neutral solvent, often are composed of organic molecules whose properties can be chemically tailored, leading to a wide variety of possible ion combinations.[3] Ionic liquid mixtures, which are ionic liquids containing more than one type of anion or cation and are also sometimes referred to as double salt ionic liquids,[7] further broaden the number of possible electrolyte compositions.[8] Recently some ionic liquid mixtures have been demonstrated experimentally and theoretically to exhibit advantages over pure ionic liquids for supercapacitor applications. For example, a 1:1 molar ratio mixture of 1-methyl-1-propylpiperidinium bis(fluorosulfonyl)imide and 1-butyl-1-methylpyrrolidinium bis(fluorosulfonyl)imide has been experimentally shown to improve supercapacitor performance at low temperatures.[1,9] At room temperature, various mixtures of ionic liquids have been shown to enhance capacitance when used in conjunction with onionlike carbon electrodes,[10,11] mesoporous carbon electrodes,[12] or mercury electrodes.[13] However, existing theoretical and computational work on ionic liquid mixtures in supercapacitors remains limited,[10,12,14,15] and there is a need for additional understanding of the mechanisms by which ionic liquid mixtures can improve supercapacitor performance.

Here, using all-atom molecular dynamics (MD) simulations, we study the effect of ionic liquid mixture composition on double-layer capacitance and ion distributions near planar carbon electrodes carrying various different charges. We choose to study ionic liquid mixtures composed of 1-ethyl-3-methylimidazolium ($EMIM^+$), bis(trifluoromethylsulfonyl)-imide ($TFSI^-$), and tetrafluoroborate (BF_4^-), with compositions ranging from pure [$EMIM^+$][$TFSI^-$] to pure [$EMIM^+$]-[BF_4^-]. These ions are commonly studied for supercapacitor applications and have been experimentally observed to increase capacitance and operating voltage window when paired with onionlike carbon electrodes.[10,16] In addition, the significant difference in the sizes of the two anions may be expected to potentially result in interesting behavior.[7]

Our simulations reveal that near uncharged electrodes, there is a significant enrichment in $TFSI^-$ relative to BF_4^- in the first interfacial layer in the ionic liquid mixtures. Using a mean-field

Received: October 23, 2018
Revised: December 13, 2018
Published: January 4, 2019

DOI: 10.1021/acs.jpcc.8b10334
J. Phys. Chem. C 2019, 123, 1610−1618

theory, we demonstrate that the relative strengths of the van der Waals interactions of the ions with the electrodes play an important role in this behavior. We also observe that the double-layer capacitance of the ionic liquid mixtures is generally intermediate between those of the two pure ionic liquids, with differences occurring primarily at the negative electrode. By examining cumulative ion densities within various distances of the electrodes, we identify different charging mechanisms in the different ionic liquids. Furthermore, in mixtures with sufficiently low mole fraction anions BF_4^-, we find that the densities of the two types of anions in the first interfacial layer exhibit opposite trends as electrode charge becomes increasingly negative, leading to an effective exchanging of the anions that provides a mechanism for capacitance enhancement. More broadly, our simulations elucidate how supercapacitor capacitance and charging mechanisms are influenced by ion−ion and ion−electrode interactions as well as differences in effective ion sizes.

2. METHODS

2.1. All-Atom Molecular Dynamics Simulations. A schematic of our simulation setup is shown in Figure 1a, and

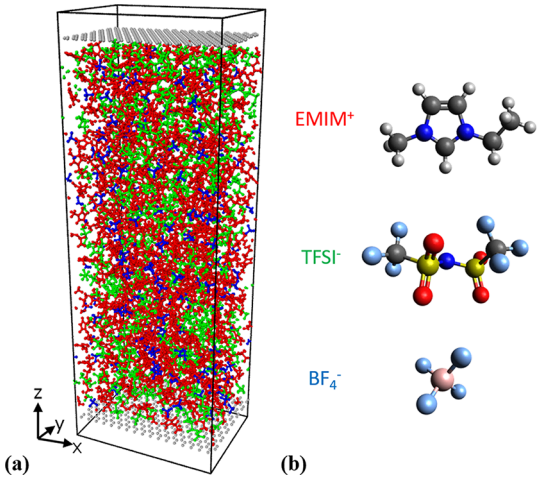

Figure 1. (a) Schematic of our simulation setup, in which an ionic liquid (here, $X = 0.5$) is placed between two graphene sheets that act as electrodes. $EMIM^+$, $TFSI^-$, BF_4^-, and electrode carbons are shown in red, green, blue, and gray, respectively. (b) Structures of the ions in the ionic liquid.

ion structures are shown in Figure 1b. Molecular dynamics simulations are performed using GPU-accelerated LAMMPS (version 11 Aug. 2017),[17−19] and initial configurations for the ionic liquid are generated using Packmol.[20] The ionic liquids are modeled using the nonpolarizable OPLS-based all-atom force field of ref 21 without scaling the charges, and the Lennard-Jones parameters for the carbon atoms of the electrode are modeled with OPLS values of $\varepsilon = 0.29288$ kJ/mol and $\sigma = 0.355$ nm.[22] The electrodes are modeled as graphene sheets with a lattice constant of $a = 0.246$ nm, spatially fixed positions, and sheet dimensions of 4.18 nm × 2.98 nm. Constant charges ranging from 0 to $\pm 0.014e$, where e is the elementary charge, are placed on each of the atoms in the electrodes to model delocalized charge injected into the electrodes, with charges of equal magnitude and opposite sign on each of the two electrodes. Although this fixed charge method does not account for the polarizability of the electrodes, we limit our study to voltages that are typical of experiments, which are low enough that the constant charge method remains a reasonable approximation for the more computationally expensive constant-potential method.[23,24] Long-range Coulombic interactions are calculated using a particle-particle particle-mesh (PPPM) solver with a slab geometry along the z direction, which is defined as the intersheet axis, as shown in Figure 1a. We use a velocity-Verlet integrator with a 1 fs time step, and periodic boundary conditions are used in the x and y directions. Our production simulations are performed at an elevated temperature of 400 K to expedite the dynamics of the system since previous MD simulations have shown that in similar systems, the capacitance does not vary significantly with temperature between approximately 300 and 400 K.[14,25] Reported average values and standard deviations of observable quantities are computed using block averaging with 1 ns long blocks.[26]

We simulate ionic liquids with compositions $X \in \{0,0.25,0.5,0.75,1\}$, where X is the mole fraction of anions that are BF_4^-, so that the ionic liquid composition is $[EMIM^+][TFSI^-]_{1-X}[BF_4^-]_X$. The number of ion pairs ranges from 291 for $X = 0$ to 485 for $X = 1$, chosen such that the final separation between the electrodes is approximately 11 nm for each of the systems. After initial assembly, systems are first equilibrated in the NVT ensemble using a stochastic velocity-rescaling thermostat applied only to the ionic liquid. The temperature is held at 600 K for at least 1 ns, ramped down to 400 K over 1 ns, and held at 400 K for 2 ns. Next, the system is simulated in the NPT ensemble for at least 2 ns at a temperature of 400 K and a pressure of 101.325 kPa, which is implemented by allowing one of the electrodes to move as a piston that experiences a specified force. Next, we fix electrode z positions based on the average z position of the piston electrode during the last 1 ns of the NPT simulation, and all subsequent simulations are performed in the NVT ensemble at 400 K. For uncharged electrodes, we perform 20 ns of equilibration. For charged electrodes, charges are ramped up to their final values over 0.5 ns, followed by 5.5 ns of equilibration at the specified charge. Production simulations are performed in the NVT ensemble for 20 ns in all cases. To improve statistical accuracy, the systems with charged electrodes are simulated twice, implemented by swapping which of the electrodes in the initial uncharged system are subsequently positively or negatively charged. In systems with uncharged electrodes, results from each of the two electrodes serve as replicates. In the mixtures, poor mixing of the ionic liquid is a significant challenge at the simulated time scales and is particularly apparent due to the presence of multiple types of anions, so additional equilibration is performed prior to production simulations. Specifically, following assembly, ionic liquid mixture systems are equilibrated in the NVT ensemble at a temperature of 600 K for 2 ns. Then, systems are simulated in the NPT ensemble at a pressure of 101.325 kPa, first for at least 4.5 ns at 600 K, then with the temperature ramped down to 400 K over 0.5 ns, and finally with the temperature held at 400 K for 3 ns. Subsequent NVT simulations are performed in the same way as desribed above.

To compute the cation−anion intermolecular interaction energies, separate MD simulations of the bulk ionic liquids $[EMIM^+][TFSI^-]$ and $[EMIM^+][BF_4^-]$ are performed. For each system, 200 ion pairs are assembled using Packmol[20] in a cubic box, and simulations are performed with periodic boundary conditions in all directions. First, the systems are

DOI: 10.1021/acs.jpcc.8b10334
J. Phys. Chem. C 2019, 123, 1610−1618

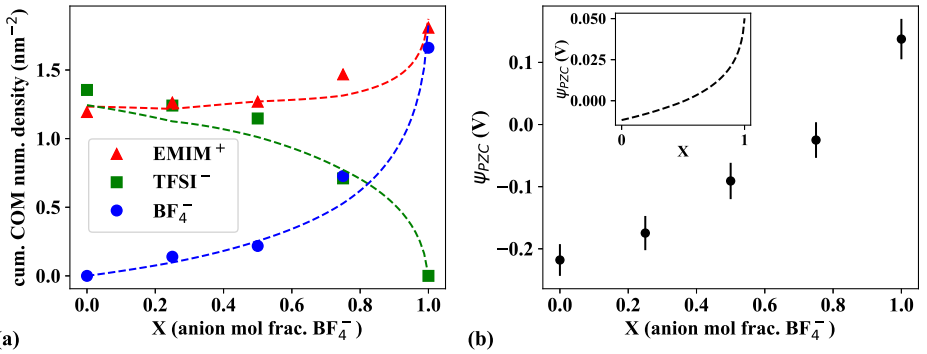

Figure 2. (a) Cumulative number density of ion COMs within 0.7 nm of uncharged electrodes, as a function of X, the mole fraction of anions that are BF_4^-. Points are from MD simulations, and dashed lines are from the mean-field theory. (b) Potential of zero charge ψ_{PZC} as a function of X, obtained from MD simulations. Inset shows ψ_{PZC} obtained from the mean-field theory. Error bars are standard deviations computed from block averaging.

simulated in the NPT ensemble using an isotropic Berendsen barostat at a pressure of 101.325 kPa and a stochastic velocity-rescaling thermostat at a temperature of 600 K for 2.5 ns, after which the temperature is ramped down to 400 K over 0.5 ns, followed by 2 ns with the temperature held at 400 K. Next, the system is simulated in the NVT ensemble for 4 ns. Using data from the last 2 ns of the NVT simulation, we compute the total intermolecular (Lennard-Jones and Coulombic) interaction energies of all cations with all anions and divide by the total number of ion pairs in order to obtain an estimate for the ion-pair interaction energy.

2.2. Mean-Field Theory. We develop a mean-field model based on the generalized Poisson–Fermi model of ref 27 in order to model ion populations near uncharged electrodes. In addition to accounting for multiple ion species and the different molar volumes of the ions, we introduce a purely attractive short-range interaction energy between each of the ions and the electrodes, which describes specific adsorption of the ions due to van der Waals forces. For our case of one type of cation and two types of anions, the concentrations of each ion species thus become

$$c_i = \frac{c_i^\infty \exp\left(\frac{-q_i e\psi - U_i(z)}{k_B T}\right)}{1 - \sum_j \nu_j c_j^\infty + \sum_j \exp\left(\frac{-q_j e\psi - U_j(r)}{k_B T}\right)\nu_j c_j^\infty} \quad (1)$$

where $c_i \in \{c_+, c_{1-}, \text{and } c_{2-}\}$ are the concentrations of each of the types of ions, q_i are the charge numbers of each of the ions, $\nu_i \in \{\nu_+, \nu_{1-}, \text{and } \nu_{2-}\}$ are the molar volumes of each of the types of ions, k_B is Boltzmann's constant, T is the temperature, e is the elementary charge, ψ is the electrostatic potential, and the bulk ion concentrations c_i^∞ obey the electroneutrality relationship $q_+ c_+^\infty + q_{1-} c_{1-}^\infty + q_{2-} c_{2-}^\infty = 0$. Thus, $X = \frac{c_{2-}^\infty}{c_{1-}^\infty + c_{2-}^\infty} = \frac{c_{2-}^\infty}{c_+^\infty}$ is the mole fraction of the anions that are type 2 in the bulk solution, which can be viewed as equivalent to the parameter X used to characterize the MD simulations. Here, the short-range attractive component of the van der Waals interaction energy of ion type i with a planar electrode is described by integration of a Lennard-Jones potential over half-space in order to model interactions with a flat wall[28] and is

$$U_i(z) = 2\pi\varepsilon_{LJ}\left[\frac{2}{45}\left(\frac{z_0}{z + z_s}\right)^9 - \frac{1}{3}\left(\frac{z_0}{z + z_s}\right)^3\right] \quad (2)$$

where z is the distance from the wall, $z_s = z_0/(5/2)^{1/6}$ is a shift so that the potential is purely attractive (since the Poisson–Fermi model considered here leads to ion density peaks at $z = 0$), z_0 is a parameter corresponding to the length scale of influence of the Lennard-Jones potential, and ε_{LJ} determines the strength of the attractive potential.

The electrostatic potential ψ is governed by Poisson's equation along the z axis (normal to the plane of the electrode)

$$\frac{d}{dz}\left(\varepsilon_r \varepsilon_0 \frac{d\psi}{dz}\right) = -e\sum_i q_i c_i \quad (3)$$

with boundary conditions

$$\left.\frac{d\psi}{dz}\right|_{z=0} = -\frac{\sigma}{\varepsilon_r \varepsilon_0}; \quad \left.\frac{d\psi}{dz}\right|_{z\to\infty} = 0 \quad (4)$$

where σ is the surface charge density of the electrode, which is 0 for an uncharged electrode, $\varepsilon_r = 10$ is the effective relative permittivity,[29] and ε_0 is the permittivity of vacuum. The equations are nondimensionalized (see the Supporting Information), discretized using finite differences, and solved iteratively for $\psi(z)$ using a fixed point method. Subsequently, $c_i(z)$ can be calculated from $\psi(z)$, and the cumulative number density in the interfacial layer can be estimated by integrating from $z = 0$ to some distance $z = z_{int}$. We use $\nu_+ c_+^\infty = \frac{\gamma}{1 + (1-X)\frac{\nu_{1-}}{\nu_+} + X\frac{\nu_{2-}}{\nu_+}}$, where $1 - \gamma$ represents the fraction of free volume, and we choose $\gamma = 0.75$ to model a fairly densely packed electrolyte, since γ is expected to be between 0.5 and 1 for most ionic liquids.[30] We denote $TFSI^-$ and BF_4^- as anions 1 and 2 respectively, and we use relative ion volumes $\frac{\nu_{1-}}{\nu_+} = 1.6$ and $\frac{\nu_{2-}}{\nu_+} = 0.22$, consistent with previous estimates for the sizes of these ions.[10] We use $z_0 = 0.35$ nm for all ions, and we integrate the computed concentration profiles over $z_{int} = 0.45$ nm. Note that these values for z_0 and z_{int} are chosen in order to yield good agreement with the MD simulations for cumulative ion densities in the interfacial layer, while they are also physically reasonable. For ε_{LJ} we use values based on the average per-ion interaction energies with uncharged electrodes obtained from our MD simulations, as described in section 3.1 below.

DOI: 10.1021/acs.jpcc.8b10334
J. Phys. Chem. C 2019, 123, 1610–1618

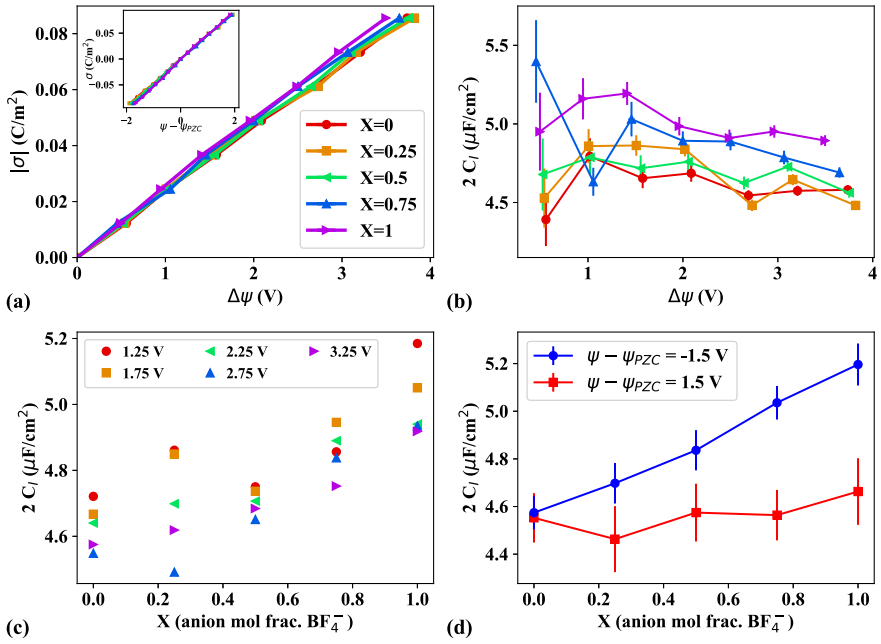

Figure 3. (a) Electrode surface charge density magnitude $|\sigma|$ as a function of total voltage across the cell $\Delta\psi$ for various ionic liquid compositions. Inset shows the charge density and voltage of the two electrodes separately. (b) Integral capacitance of the full cell as a function of cell voltage for various ionic liquid compositions, plotted with the same colors and markers as in (a). (c) Integral capacitance of the full cell as a function of X at five constant cell potentials ranging from 1.25 to 3.25 V. (d) Integral capacitance of each electrode as a function of X at electrode voltages of −1.5 and 1.5 V. Error bars are standard deviations computed from block averaging.

3. RESULTS AND DISCUSSION

3.1. Ion Adsorption at Uncharged Electrodes. First, we consider uncharged electrodes and examine the populations of ions adsorbed in the first interfacial layer for various electrolyte compositions. The points in Figure 2a show the cumulative center of mass (COM) ion density within 0.7 nm of the electrodes, which corresponds to the first adsorbed layer of ions, as a function of composition, from the MD simulations. In the mixtures, we observe a significant enrichment in the number of $TFSI^-$ ions relative to the number of BF_4^- ions, compared to the bulk composition. This enrichment occurs due to the significantly larger van der Waals attraction to the electrodes of the $TFSI^-$ ions compared to the BF_4^- ions. From our MD simulations, the average per-ion interaction energy with the wall can be estimated for each type of ion by summing the Lennard-Jones interaction energies of all ions within 1.3 nm of the electrodes (the cutoff distance) and dividing by the total number of ion COMs within that cutoff distance. We find that the average per-ion Lennard-Jones interaction energies with the wall are −19 kJ/mol for $EMIM^+$, −22 kJ/mol for $TFSI^-$, and −6 kJ/mol for BF_4^-. Using smaller cutoff distances results in larger per-ion interaction energy magnitudes but similar ratios between the energies of the different ions. These energies are correlated with effective ion size, with larger ions experiencing greater attractive interactions with the electrodes.

Using a Poisson−Fermi mean-field model (described in section 2.2) in which we include different attractive energies with the wall for each of the types of ions, we are able to produce similar behavior to the cumulative interfacial ion adsorption densities observed in the MD simulations, as shown by the dashed curves in Figure 2a. Note that the close agreement arises because z_0 and z_{int} in the mean-field model are effectively fitting parameters, and the mean-field model used here should only be interpretted as yielding qualitative predictions since it is a highly simplified description of the system. The potential of zero charge (PZC) for each ionic liquid composition can also be extracted from our MD simulations (see section 3.2 below for details), and the PZCs are shown in Figure 2b. We observe that the PZC transitions from negative to positive as X varies from 0 to 1, consistent with previous MD simulations of each of the pure ionic liquids.[31,32] As shown in the inset of Figure 2b, our mean-field model exhibits the same qualitative trend as the MD simulations, with a transition from negative to positive values as X increases from 0 to 1. Here, agreement between the mean-field model and MD simulations is not quantitative because the electrostatic potential is relatively sensitive to the details of ion arrangements, which are not fully captured by the mean-field theory.

Consistent with our findings, experiments with ionic liquids at a mercury electrode have observed a more positive PZC with decreasing anion size.[13] On the other hand, existing classical density functional theory models[33] that treat ions as charged hard spheres and do not fully consider ion−electrode van der Waals interactions have predicted contrasting trends in ion adsorption densities and PZCs.[10,15,34] Our results suggest that ion adsorption densities near uncharged electrodes, and consequently the PZC (which is affected by which type of ion preferentially resides closer to the electrode), strongly depend on the intensity of the ions' respective van der Waals interactions with the walls.

3.2. Capacitance and Ion Adsorption Densities near Charged Electrodes. Next, we explore the behavior of systems with electrodes carrying nonzero surface charges. In order to determine the voltage and double-layer capacitance of the electrodes from the MD simulations, we compute the potential ψ across the cell by solving Poisson's equation in one dimension:

DOI: 10.1021/acs.jpcc.8b10334
J. Phys. Chem. C 2019, 123, 1610−1618

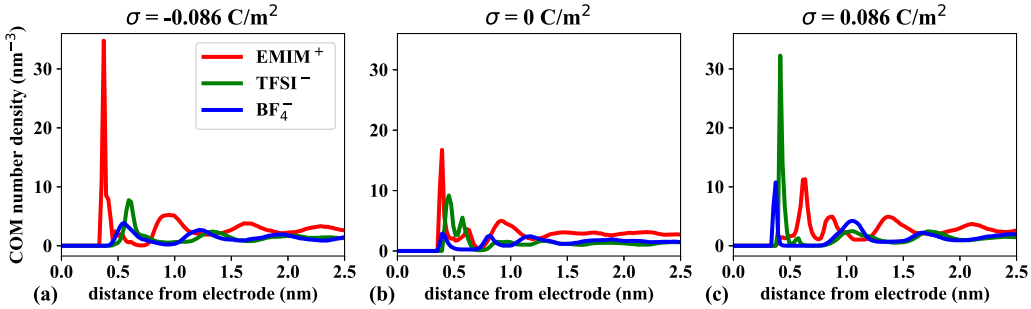

Figure 4. Representative ion COM number density profiles for a $X = 0.5$ ionic liquid mixture near electrodes carrying surface charge densities of (a) $\sigma = -0.086$ C/m^2, (b) $\sigma = 0$ C/m^2, and (c) $\sigma = 0.086$ C/m^2. Different colors represent different species of ions (same legend applies to all subfigures).

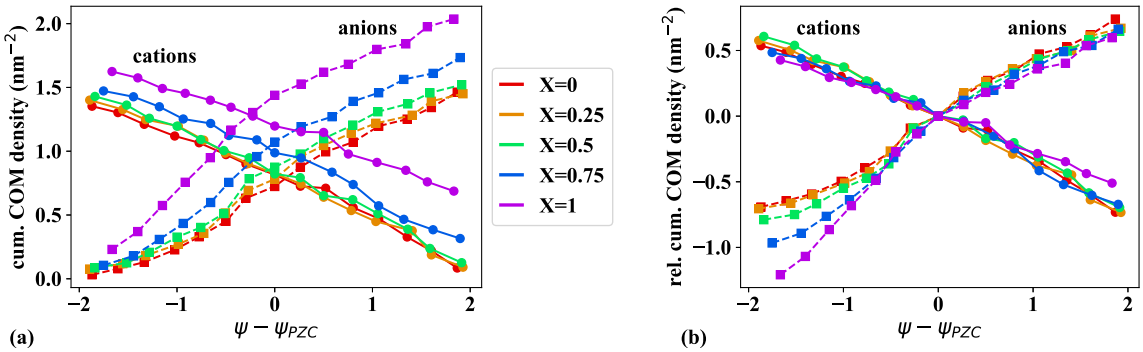

Figure 5. (a) Cumulative ion COM number densities within 0.5 nm of the electrodes for various ionic liquid compositions. (b) Cumulative ion COM number densities within 0.5 nm of the electrodes relative to their zero-charge values. In all plots, cation densities are shown as circles connected by solid lines while anion densities are shown as squares connected by dashed lines.

$$\frac{d^2\psi}{dz^2} = -\frac{\rho}{\varepsilon_0} \tag{5}$$

where the charge density ρ is calculated by histogramming the charges of the atoms as a function of position in z and averaging over time. Here we define the PZC as the difference between the electrode potential and the potential in the bulk of the electrolyte for electrodes with zero charge: $\psi_{PZC} = \psi_{el,0} - \psi_{bulk,0}$. From the applied surface charge density σ and the measured potential difference across the entire cell $\Delta\psi$, we can calculate the integral capacitance of the full cell as $C_I = \frac{|\sigma|}{\Delta\psi}$. We can also calculate integral capacitances for each of the electrodes separately via $2C_I = \frac{\sigma}{\psi - \psi_{PZC}}$, where ψ is the potential drop between the electrode and the bulk electrolyte. Figure 3a shows $|\sigma|$ on each electrode vs $\Delta\psi$ for various values of X, while the inset shows σ as a function of $\psi - \psi_{PZC}$. The behavior is quite similar for all of the ionic liquid compositions, indicating that there are only small differences in the integral capacitances of the various ionic liquids.

As shown in Figure 3b, the total integral capacitance is overall highest for $X = 1$, and none of the mixtures exhibit a higher integral capacitance than the best-performing pure composition. To provide a more direct comparison of the different electrolyte compositions, we plot in Figure 3c the total integral capacitances intepolated to five values of constant cell potential ranging from 1.25 to 3.25 V, showing a trend of increasing capacitance as X increases. As shown in Figure 3d, when we consider the integral capacitance of each electrode separately (also see Figure S1), we find that most of the variation in integral capacitance with X occurs at the negative electrode, while the positive electrode only shows a very weakly increasing trend with X and tends to have a lower integral capacitance. Interestingly, the observation of higher capacitance at the negative than positive electrode for $X = 1$ is consistent with previously reported atomistic MD simulations[32] but is not predicted by mean-field theories, which instead simply predict higher capacitance on the electrode that adsorbs the smaller ion (in this case, the positive electrode, where the smaller BF_4^- ions adsorb).[35,36]

To understand the mechanisms behind the observed capacitance behavior, we can examine the ion adsorption profiles near the electrodes. Figure 4 shows ion COM number densities near electrodes carrying various surface charges, for the $X = 0.5$ mixture, as an illustrative example. As expected,[32,37] counterions adsorb while co-ions desorb upon charging, and alternating layers rich in cations and anions form near charged electrodes, persisting over several nanometers.

To quantify the accumulation of different types of ions near the electrodes, we can compute the cumulative ion COM number density within a specified distance d of the electrodes, which corresponds to integrating the peaks in Figure 4 from 0 to some distance d. First, we consider ion densities within $d = 0.5$ nm of the electrodes, which is chosen to only include the ions within the first interfacial layer that are closest to the electrodes (i.e., ions lying flat against the electrodes). These ions are expected to have the greatest influence on the capacitance because spatial oscillations in the charge density, which determine the potential, decay rapidly to zero within less than 1 nm from the electrodes, despite the longer-range layering seen in the COM density profiles (see Figure S2 and similar observations in refs 37 and 32).

DOI: 10.1021/acs.jpcc.8b10334
J. Phys. Chem. C 2019, 123, 1610−1618

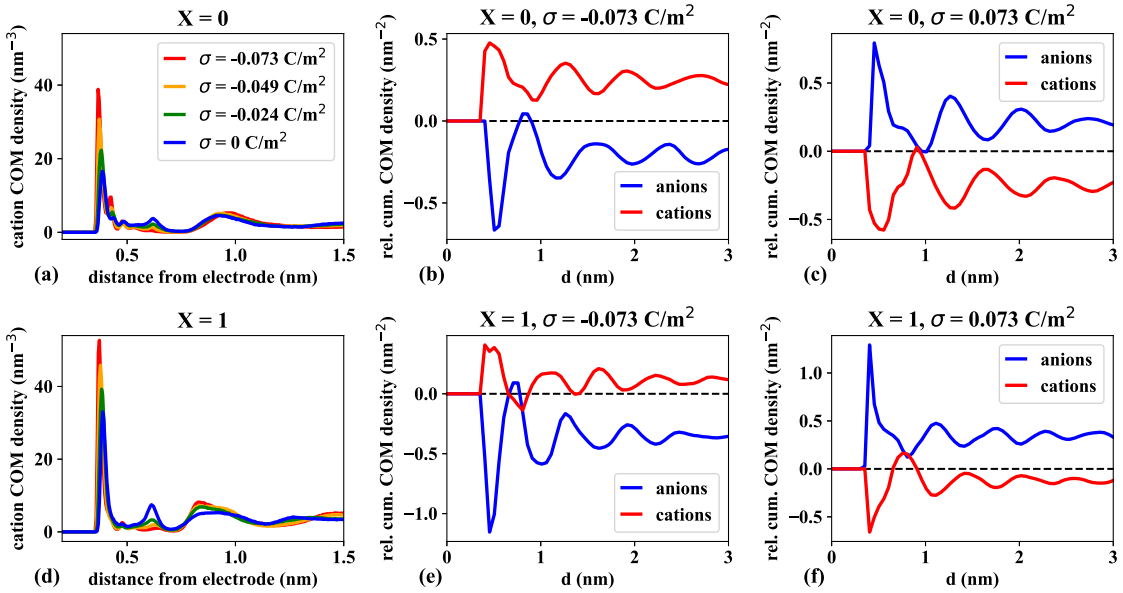

Figure 6. (a, d) COM number density of $EMIM^+$ for various different electrode surface charge densities σ. (b, e) Cumulative COM ion number densities within a distance d from an electrode carrying a charge of σ =−0.073 C/m^2, relative to the values near an uncharged electrode. (c, f) Cumulative COM ion number densities within a distance d from an electrode carrying a charge of σ = 0.073 C/m^2, relative to the values near an uncharged electrode. In (a–c), X = 0, while in (d–f), X = 1.

Figure 5a shows the cumulative COM number densities of cations and anions within 0.5 nm of the electrodes as a function of electrode voltage for various different electrolyte compositions, showing expected trends of cations and anions adsorbing or desorbing depending on whether they are counterions or co-ions. Since capacitance is determined by changes relative to the uncharged state, we plot in Figure 5b the cumulative ion densities within 0.5 nm of the electrodes shifted by their zero-charge values. As shown in Figure 5b, at negatively charged electrodes, the relative amount of anion desorption clearly increases as X increases, which partially explains the increase in capacitance with X at the negative electrode seen in Figure 3d. This behavior may be attributed to the smaller effective size of the BF_4^- anion than the $TFSI^-$ anion, which allows for a higher packing density and closer approach near uncharged electrodes and thus greater relative desorption upon negatively charging the electrode.

More subtly, Figure 5b also shows that relative cation adsorption near negatively charged electrodes tends to be greater for the X = 0.25 and X = 0.5 mixtures than for both of the pure ionic liquids. This nonintermediate mixture behavior will be discussed in greater detail in section 3.3 below. At the positive electrode, no significant trends with respect to ionic liquid composition are observed, consistent with the weak dependence on X of the positive electrode capacitance seen in Figure 3d. Despite the different anions adsorbing on the positive electrode, the relative cumulative density behavior of the different compositions is similar due to the fact that the smaller BF_4^- anions are accompanied by a higher density of $EMIM^+$ cations, eliminating any advantages in ion adsorption density that may have been expected due to the smaller size of the BF_4^-.

While the relative cumulative cation densities within 0.5 nm of the electrodes correlate well with the characterized electrode integral capacitances, further understanding of the different charging mechanisms in different ionic liquids can be gained by also examining the behavior of ions within a greater distance from the electrodes. To highlight variations, here we focus on the two pure ionic liquids and first consider as an illustrative example the cation COM number density profiles near negatively charged electrodes, as shown in Figures 6a and d for X = 0 (pure $[EMIM^+][TFSI^-]$) and X = 1 (pure $[EMIM^+][BF_4^-]$) respectively. The peak in density closest to the electrode corresponds to $EMIM^+$ ions lying flat against the electrode, while the peak near 0.6 nm corresponds to $EMIM^+$ oriented perpendicularly to the electrode, with one alkyl group adjacent to the electrode and the other pointing away so that the ring of the molecule is elevated and tilted from the electrode plane, as determined by separately visualizing ions with COMs in certain regions. Figures 6a and d show that as the electrode becomes increasingly negatively charged, there is a noticeably greater decrease in the size of the peak near 0.6 nm for X = 1 compared to for X = 0, which implies that for X = 1 there is a larger degree of cation reorientation within the first interfacial layer. Indeed, all of the ionic liquid compositions studied here exhibit significant cation reorientation within the first interfacial layer upon charging of the electrodes (see Figure S3).

To further quantify ion density changes, we next plot the cumulative ion COM number densities relative to their zero-charge values as a function of considered distance d from the electrode, as shown in Figures 6b, c, e, f. Figures 6b, e show that at the negative electrode, for X = 0 charging is overall driven by a greater amount of cation adsorption and less anion desorption than for X = 1. Likewise, Figures 6c, f show that at the positive electrode, for X = 0 there is overall greater cation desorption and less anion adsorption than for X = 1. These results suggest that for each ionic liquid, one of the ion species can experience greater changes in cumulative density in response to electrode charging than the other ion species. In particular, here we observe greater changes in cumulative densities of the smaller ion in each ionic liquid, which may reflect a preference of the larger ion to instead reorient rather than adsorb/desorb. These findings are consistent with

DOI: 10.1021/acs.jpcc.8b10334
J. Phys. Chem. C 2019, 123, 1610–1618

previous MD simulations using different electrode structures, which showed that in supercapacitors with [EMIM$^+$][TFSI$^-$] as the electrolyte, the smaller EMIM$^+$ ion is more "active" and adsorbs/desorbs more than the larger TFSI$^-$ ion, while in other ionic liquids with a smaller anion than cation, the anion was found to be more "active."[5]

The plots of relative cumulative ion density as a function of d in Figure 6 also demonstrate the complex nature of ion restructuring near charged electrodes. For example, Figure 6e shows that for X = 1, the relative cumulative cation density near a negatively charged electrode falls below zero near d = 0.7 nm, indicating that within 0.7 nm, there is actually a small net loss in cumulative number of cations upon negatively charging the electrode, despite the fact that the cations are counterions. This suggests that the increases in cumulative cation density within d < 0.7 nm are primarily driven by reorientation and local reorganization of the cations. In contrast, Figure 6b shows that for X = 0, the change in cumulative cation density always remains positive near a negatively charged electrode, suggesting a greater role of ion adsorption from the bulk electrolyte.

3.3. Effective Ion Exchanging Phenomenon in Certain Mixtures. Next, we focus on behavior specific to ionic liquid mixtures. To better understand the enhanced cation adsorption near the negative electrode shown in Figure 5 for the mixtures with X = 0.25 and X = 0.5, we examine the cumulative densities of each type of ion within 0.7 nm of the electrodes, as shown in Figure 7, for the X = 0.5 mixture. Here

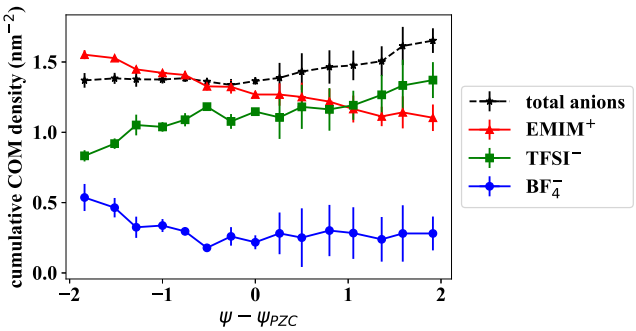

Figure 7. Cumulative ion COM number densities within d = 0.7 nm of the electrodes for X = 0.5. TFSI$^-$ and BF$_4^-$ densities vary differently as a function of electrode potential, leading to an effective exchanging of the two types of anions. Here, the range of the error bars corresponds to the difference between the two replicate simulations.

we choose to consider d = 0.7 nm in order to include both counterions and co-ions in the first interfacial layer over the range of electrode surface charges considered. While the cation density expectedly increases or decreases with electrode voltage depending on whether EMIM$^+$ is a counterion or co-ion, the two types of anions display distinctly different behavior. With increasingly negative electrode voltages, the TFSI$^-$ density decreases while the BF$_4^-$ density increases. On the other hand, an increasingly positive electrode voltage leads to an increase in TFSI$^-$ density and no significant change in BF$_4^-$ density.

This effective exchanging of the two types of anions near negatively charged electrodes occurs due to the different interaction energies and sizes of the two anions. The intermolecular attraction between EMIM$^+$ and BF$_4^-$ is greater than that of EMIM$^+$ and TFSI$^-$, which can qualitatively be understood to arise due to the closer approach of the smaller BF$_4^-$ anion to the cation. Quantitatively, we compute cation−anion intermolecular interaction energies from simulations of bulk pure ionic liquids (as described in section 2.1), yielding ion-pair interaction energy estimates of −346 kJ/mol for [EMIM$^+$][TFSI$^-$] and −439 kJ/mol for [EMIM$^+$][BF$_4^-$]. Thus, the increase in cation density near negatively charged electrodes also leads to a relative increase in nearby BF$_4^-$ density. Additionally, as the anions move farther away from negatively charged electrodes, their attractive van der Waals interactions with the electrodes become less significant, so the driving force for enrichment in TFSI$^-$ (discussed in section 3.1) is reduced. Finally, Figures 4a, b show that negatively charging the electrode appears to cause the first two BF$_4^-$ density peaks nearest the electrode (peaks near 0.4 and 0.8 nm near the uncharged electrode) to merge into one, thus increasing the BF$_4^-$ density in the first interfacial layer due to the layering distances dictated by the ion sizes.

An important consequence of the increase in BF$_4^-$ density in the first interfacial layer with increasingly negative electrode charge is that cation adsorption near the electrode is enhanced since the smaller size of BF$_4^-$ than TFSI$^-$ leads to a higher ion number density. This increase in cation adsorption in the ionic liquid mixtures provides a mechanism for capacitance enhancement since the ions closest to the electrodes have the greatest influence on the capacitance. We note that the prominence of this effective anion exchanging phenomenon is greater for lower values of X, so that mixtures with sufficiently high mole fractions of BF$_4^-$ exhibit no significant anion exchanging in the first interfacial layer (see Figure S4). This occurs because the effective exchanging of the anions is largely driven by changes in the density of the cations, and more EMIM$^+$ adsorption occurs at the negative electrode in the presence of TFSI$^-$ than in the presence of BF$_4^-$, as discussed in section 3.2 above. Additionally, ionic liquids with a greater fraction of TFSI$^-$ (lower X) have wider spacing between ion layers near the electrodes, favoring greater increases in the amount of BF$_4^-$ between the cation layers. We expect that the effective anion exchanging effect would be more prominent in ionic liquids with greater differences between the sizes of the two anion species.

Near positively charged electrodes, one might expect that, by the same ion−ion interaction mechanism as near negatively charged electrodes, desorption of EMIM$^+$ ions would lead to a reduction in BF$_4^-$ density and an increase in TFSI$^-$ density in the first interfacial layer. However, no significant effective anion exchanging upon positively charging the electrode is observed in Figure 7. A likely reason for this is that ion−electrode interactions become more important when the anions are counterions due to their close contact with the electrodes, and the small BF$_4^-$ anion is expected to be strongly attracted to positively charged electrodes due to its close approach to the surface. In addition, we note that the low density of BF$_4^-$ near uncharged electrodes limits how much BF$_4^-$ can desorb upon charging even if there were a driving force for desorption.

From a practical standpoint, even if effective anion exchanging were to occur at the positive electrode, it would not necessarily improve the positive electrode capacitance since any benefits from enhancement in cation desorption would be offset by the reduction in adsorption of the smaller anion, which is expected to have a large impact on capacitance due to its close approach to positively charged electrodes.

DOI: 10.1021/acs.jpcc.8b10334
J. Phys. Chem. C 2019, 123, 1610−1618

Therefore, in order to maximize improvements in overall cell capacitance of ionic liquid mixtures via the anion exchanging phenomenon identified here, the capacitance of the negative electrode should be lower than that of the positive electrode so that improvements in the negative electrode capacitance would significantly impact overall cell capacitance.

4. CONCLUSION

Here we have performed all-atom MD simulations of $[EMIM^+][TFSI^-]_{1-X}[BF_4^-]_X$, with X ranging from 0 to 1, near planar carbon electrodes carrying various surface charges. In the first interfacial layer near uncharged electrodes, we find that $TFSI^-$ adsorbs preferentially over BF_4^- in mixtures due to its greater van der Waals attraction to the electrodes. We also observe that the total integral capacitance of the cell generally increases with the amount of BF_4^- in the ionic liquid, with most of the differences occurring at the negative rather than the positive electrode. By analyzing changes in cumulative ion densities in the vicinity of the electrodes, we find that in each pure ionic liquid, upon charging the electrodes the smaller ion tends to experience overall greater changes in cumulative density than the larger ion, which instead tends to reorient and locally restructure. Finally, in the ionic liquid mixtures we identify a mechanism for capacitance enhancement at the negative electrode that occurs via an effective exchanging of the two types of anions, which enhances cation adsorption, driven by differences in the effective ion sizes and intermolecular interactions. We find that the extent of anion exchanging is greatest in mixtures with lower mole fractions of BF_4^-, and we note that capacitance enhancements via this mechanism only occur at the negative electrode, suggesting maximum overall gains in systems where the total cell capacitance is limited by the negative electrode.

Overall, our work provides insight into the behavior of ionic liquid mixtures near charged surfaces. Although our simulations do not yield a higher integral capacitance for any of the mixtures relative to the pure ionic liquids, as was observed in the experiments of ref 10, we note that the effective anion exchanging phenomenon identified here, which is more prominent at lower mole fractions of BF_4^-, could play a role in the capacitance enhancement at $X = 0.2$ reported in ref 10. Additionally, there are a variety of phenomena that may be present in experimental supercapacitor cells but are not modeled in our simulations, and our results suggest that at least some of these factors may significantly impact experimentally measured capacitances. For example, in experiments there may be trace amounts of water that preferentially accumulate at the electrode interface,[38] and functional groups or contaminants such as hydrocarbons adsorbed from the ambient environment[39] may be present on electrode surfaces. Furthermore, capacitances measured via cyclic voltammetry arise from a dynamic charging process, whereas our simulations characterize a system in equilibrium. We also note that our simulations do not explicitly account for polarizability of either the electrodes or the ions in the electrolyte, and we model the electrodes as planar graphene sheets, which may not be a good description of structures such as the onionlike carbon electrodes of ref 10. Nonetheless, all-atom MD simulations offer significant advantages over simplified continuum models since our simulations are able to capture the effects of detailed atomistic structures and interactions of specific ions with the electrodes, including the reorientation of ions near the electrodes upon charging, for example.

Our results suggest that in order to achieve more substantial improvements in supercapacitor energy density, it will be necessary to not only tune the electrolyte composition but also modify electrode properties, for example via surface functionalization, doping, or varying the nanoporous electrode structure. Here we have revealed how differing ion−ion and ion−electrode interactions as well as differences in the effective sizes of the various species in ionic liquid mixtures can influence the interfacial organization of ions near uncharged and charged electrodes, which in turn affects double-layer capacitances. These advances in the understanding of charging mechanisms can be used to develop new strategies for engineering improved supercapacitors.

■ ASSOCIATED CONTENT

Supporting Information

The Supporting Information is available free of charge on the ACS Publications website at DOI: 10.1021/acs.jpcc.8b10334.

Details on nondimensionalization of the mean-field model, integral capacitances of the separate electrodes, example charge density and potential profiles near a charged electrode, cation ring orientation as a function of electrode potential, and cumulative COM densities in the first interfacial layer for additional mixture compositions (PDF)

■ AUTHOR INFORMATION

Corresponding Author

*E-mail: alta.fang@nist.gov.

ORCID

Alta Fang: 0000-0002-8896-9427

Alex Smolyanitsky: 0000-0002-4378-8155

Notes

This work is a contribution of the National Institute of Standards and Technology, an agency of the U.S. government. Not subject to copyright in the USA. Trade names are provided only to specify procedures adequately and do not imply endorsement by the National Institute of Standards and Technology. Similar products by other manufacturers may be found to work as well or better.

The authors declare no competing financial interest.

■ ACKNOWLEDGMENTS

This research was performed while A.F. held a National Research Council (NRC) Postdoctoral Research Associateship at the National Institute of Standards and Technology (NIST). Authors gratefully acknowledge support from the Materials Genome Initiative.

■ REFERENCES

(1) Tsai, W.-Y.; Lin, R.; Murali, S.; Zhang, L. L.; McDonough, J. K.; Ruoff, R. S.; Taberna, P.-L.; Gogotsi, Y.; Simon, P. Outstanding performance of activated graphene based supercapacitors in ionic liquid electrolyte from −50 to 80 C. *Nano Energy* **2013**, *2*, 403−411.

(2) Gogotsi, Y. Not just graphene: The wonderful world of carbon and related nanomaterials. *MRS Bull.* **2015**, *40*, 1110−1121.

(3) Vatamanu, J.; Borodin, O.; Olguin, M.; Yushin, G.; Bedrov, D. Charge storage at the nanoscale: understanding the trends from the molecular scale perspective. *J. Mater. Chem. A* **2017**, *5*, 21049−21076.

(4) Yu, Z.; Tetard, L.; Zhai, L.; Thomas, J. Supercapacitor electrode materials: nanostructures from 0 to 3 dimensions. *Energy Environ. Sci.* **2015**, *8*, 702−730.
(5) Forse, A. C.; Merlet, C.; Griffin, J. M.; Grey, C. P. New perspectives on the charging mechanisms of supercapacitors. *J. Am. Chem. Soc.* **2016**, *138*, 5731−5744.
(6) Salanne, M.; Rotenberg, B.; Naoi, K.; Kaneko, K.; Taberna, P.-L.; Grey, C. P.; Dunn, B.; Simon, P. Efficient storage mechanisms for building better supercapacitors. *Nat. Energy* **2016**, *1*, 16070.
(7) Chatel, G.; Pereira, J. F.; Debbeti, V.; Wang, H.; Rogers, R. D. Mixing ionic liquids − "simple mixtures" or "double salts"? *Green Chem.* **2014**, *16*, 2051−2083.
(8) Niedermeyer, H.; Hallett, J. P.; Villar-Garcia, I. J.; Hunt, P. A.; Welton, T. Mixtures of ionic liquids. *Chem. Soc. Rev.* **2012**, *41*, 7780−7802.
(9) Lin, R.; Taberna, P.-L.; Fantini, S.; Presser, V.; Pérez, C. R.; Malbosc, F.; Rupesinghe, N. L.; Teo, K. B. K.; Gogotsi, Y.; Simon, P. Capacitive energy storage from −50 to 100 °C using an ionic liquid electrolyte. *J. Phys. Chem. Lett.* **2011**, *2*, 2396−2401.
(10) Lian, C.; Liu, K.; Van Aken, K. L.; Gogotsi, Y.; Wesolowski, D. J.; Liu, H.; Jiang, D.; Wu, J. Enhancing the capacitive performance of electric double-layer capacitors with ionic liquid mixtures. *ACS Energy Lett.* **2016**, *1*, 21−26.
(11) Osti, N. C.; Gallegos, A.; Dyatkin, B.; Wu, J.; Gogotsi, Y.; Mamontov, E. Mixed ionic liquid improves electrolyte dynamics in supercapacitors. *J. Phys. Chem. C* **2018**, *122*, 10476−10481.
(12) Wang, X.; Mehandzhiyski, A. Y.; Arstad, B.; Van Aken, K. L.; Mathis, T. S.; Gallegos, A.; Tian, Z.; Ren, D.; Sheridan, E.; Grimes, B. A.; et al. Selective charging behavior in an ionic mixture electrolyte-supercapacitor system for higher energy and power. *J. Am. Chem. Soc.* **2017**, *139*, 18681−18687.
(13) Costa, R.; Voroshylova, I. V.; Cordeiro, M. N. D.; Pereira, C. M.; Silva, A. F. Enhancement of differential double layer capacitance and charge accumulation by tuning the composition of ionic liquids mixtures. *Electrochim. Acta* **2018**, *261*, 214−220.
(14) Li, S.; Feng, G.; Fulvio, P. F.; Hillesheim, P. C.; Liao, C.; Dai, S.; Cummings, P. T. Molecular dynamics simulation study of the capacitive performance of a binary mixture of ionic liquids near an onion-like carbon electrode. *J. Phys. Chem. Lett.* **2012**, *3*, 2465−2469.
(15) Lian, C.; Liu, H.; Wu, J. Ionic liquid mixture expands the potential window and capacitance of a supercapacitor in tandem. *J. Phys. Chem. C* **2018**, *122*, 18304−18310.
(16) Van Aken, K. L.; Beidaghi, M.; Gogotsi, Y. Formulation of ionic-liquid electrolyte to expand the voltage window of super-capacitors. *Angew. Chem.* **2015**, *127*, 4888−4891.
(17) Plimpton, S. Fast parallel algorithms for short-range molecular dynamics. *J. Comput. Phys.* **1995**, *117*, 1−19.
(18) Brown, W. M.; Wang, P.; Plimpton, S. J.; Tharrington, A. N. Implementing molecular dynamics on hybrid high performance computers − short range forces. *Comput. Phys. Commun.* **2011**, *182*, 898−911.
(19) Brown, W. M.; Kohlmeyer, A.; Plimpton, S. J.; Tharrington, A. N. Implementing molecular dynamics on hybrid high performance computers − Particle-particle particle-mesh. *Comput. Phys. Commun.* **2012**, *183*, 449−459.
(20) Martínez, L.; Andrade, R.; Birgin, E. G.; Martínez, J. M. PACKMOL: a package for building initial configurations for molecular dynamics simulations. *J. Comput. Chem.* **2009**, *30*, 2157−2164.
(21) Doherty, B.; Zhong, X.; Gathiaka, S.; Li, B.; Acevedo, O. Revisiting OPLS force field parameters for ionic liquid simulations. *J. Chem. Theory Comput.* **2017**, *13*, 6131−6145.
(22) Jorgensen, W. L.; Maxwell, D. S.; Tirado-Rives, J. Development and testing of the OPLS all-atom force field on conformational energetics and properties of organic liquids. *J. Am. Chem. Soc.* **1996**, *118*, 11225−11236.
(23) Wang, Z.; Yang, Y.; Olmsted, D. L.; Asta, M.; Laird, B. B. Evaluation of the constant potential method in simulating electric double-layer capacitors. *J. Chem. Phys.* **2014**, *141*, 184102.
(24) Merlet, C.; Péan, C.; Rotenberg, B.; Madden, P. A.; Simon, P.; Salanne, M. Simulating supercapacitors: can we model electrodes as constant charge surfaces? *J. Phys. Chem. Lett.* **2013**, *4*, 264−268.
(25) Feng, G.; Li, S.; Atchison, J. S.; Presser, V.; Cummings, P. T. Molecular insights into carbon nanotube supercapacitors: capacitance independent of voltage and temperature. *J. Phys. Chem. C* **2013**, *117*, 9178−9186.
(26) Frenkel, D.; Smit, B. *Understanding molecular simulation: From algorithms to applications*, 2nd ed.; Elsevier: Amsterdam, 2002.
(27) Tresset, G. Generalized Poisson-Fermi formalism for investigating size correlation effects with multiple ions. *Phys. Rev. E* **2008**, *78*, 061506.
(28) Forsman, J.; Woodward, C. E.; Trulsson, M. A classical density functional theory of ionic liquids. *J. Phys. Chem. B* **2011**, *115*, 4606−4612.
(29) Bazant, M. Z.; Storey, B. D.; Kornyshev, A. A. Double layer in ionic liquids: Overscreening versus crowding. *Phys. Rev. Lett.* **2011**, *106*, 046102.
(30) Fedorov, M. V.; Kornyshev, A. A. Ionic liquids at electrified interfaces. *Chem. Rev.* **2014**, *114*, 2978−3036.
(31) Vatamanu, J.; Borodin, O.; Bedrov, D.; Smith, G. D. Molecular dynamics simulation study of the interfacial structure and differential capacitance of alkylimidazolium bis (trifluoromethanesulfonyl) imide [C n mim][TFSI] ionic liquids at graphite electrodes. *J. Phys. Chem. C* **2012**, *116*, 7940−7951.
(32) Jo, S.; Park, S.-W.; Shim, Y.; Jung, Y. Effects of alkyl chain length on interfacial structure and differential capacitance in graphene supercapacitors: a molecular dynamics simulation study. *Electrochim. Acta* **2017**, *247*, 634−645.
(33) Note: the classical density functional theory mentioned here involves classical fluid densities and is not the quantum electronic structure modeling technique that is commonly referred to simply as density functional theory.
(34) Neal, J. N.; Van Aken, K.; Gogotsi, Y.; Wesolowski, D. J.; Wu, J. Self-amplified surface charging and partitioning of ionic liquids in nanopores. *Phys. Rev. Appl.* **2017**, *8*, 034018.
(35) Fedorov, M. V.; Kornyshev, A. A. Ionic liquid near a charged wall: Structure and capacitance of electrical double layer. *J. Phys. Chem. B* **2008**, *112*, 11868−11872.
(36) Lauw, Y.; Horne, M.; Rodopoulos, T.; Nelson, A.; Leermakers, F. Electrical double-layer capacitance in room temperature ionic liquids: ion-size and specific adsorption effects. *J. Phys. Chem. B* **2010**, *114*, 11149−11154.
(37) Paek, E.; Pak, A. J.; Hwang, G. S. A computational study of the interfacial structure and capacitance of graphene in [BMIM][PF6] ionic liquid. *J. Electrochem. Soc.* **2013**, *160*, A1−A10.
(38) Feng, G.; Jiang, X.; Qiao, R.; Kornyshev, A. A. Water in ionic liquids at electrified interfaces: The anatomy of electrosorption. *ACS Nano* **2014**, *8*, 11685−11694.
(39) Li, Z.; Kozbial, A.; Nioradze, N.; Parobek, D.; Shenoy, G. J.; Salim, M.; Amemiya, S.; Li, L.; Liu, H. Water protects graphitic surface from airborne hydrocarbon contamination. *ACS Nano* **2016**, *10*, 349−359.

DOI: 10.1021/acs.jpcc.8b10334
J. Phys. Chem. C 2019, 123, 1610−1618